RSC Advances

PAPER

View Article Online
View Journal | View Issue

Cite this: *RSC Adv.*, 2024, **14**, 32883

Functionalizable poly-terthiophene/Cu_2O heterojunction constructed *in situ* for sensitive photoelectrochemical detection of long non-coding RNA markers†

Xuehui Pang, *[a] Rui Liu,[a] Xiaoyi Lv,[ab] Wenjun Lu,[ab] Lebin Sun,[ab] Qiuyan Wang,[ab] Zhen Li,[d] Qing Kang,[d] Jiandong Xie,[a] Yingxin Pang*[c] and Feimeng Zhou*[a]

Received 19th July 2024
Accepted 11th October 2024

DOI: 10.1039/d4ra05238b

rsc.li/rsc-advances

A photoelectrochemical (PEC) sensor based on the poly-2,2,5,2-terthiophene (pTTh)/Cu_2O heterojunction was constructed and applied for the detection of long non-coding RNA (lncRNA) TROJAN, a biomarker of triple-negative breast cancer. Cu_2O and pTTh were electrodeposited *in situ* and sequentially onto an indium tin oxide substrate. The bandgap of the resultant type II heterojunction was measured spectroscopically and the morphology was found to effectively separate photogenerated holes from electrons. A photocurrent density as high as 250 μA cm^{-2} was attained, which is about three times higher than those of only pTTh or Cu_2O. Owing to the close contact between pTTh and Cu_2O, this PEC sensor is highly stable. Oligonucleotide probes for lncRNA can be cross-linked to carboxyl moieties of mercaptopropionic acid molecules adsorbed on pTTh/Cu_2O. The desirable band structure and the high density of probe molecules collectively yielded a linear range of 0.1–10 000 pM. Our PEC sensor has been demonstrated to be amenable for detection of lncRNA markers with excellent analytical performance.

1 Introduction

With improved diagnoses and modalities, early identification and precise treatments of cancers have become possible and the survival rates of patients are enhanced.[1,2] Methods such as enzyme-linked immunosorbent assay,[3] fluorescence,[4,5] surface-enhanced Raman scattering,[6,7] surface plasmon resonance,[8,9] electrochemical methods,[10–14] real-time quantitative polymerase chain reaction,[15] and various electrochemical methods[10] have shown promise in cancer biomarker detection. Many studies have reported that long non-coding RNAs (lncRNAs) carried by exosomes can be used to diagnose cancer subtypes and assess prognosis.[16–20] Recent research has shown that a lncRNA termed as TROJAN is expressed in exosomes and cells of the triple-negative breast cancer.[20] Its expression is associated with poor prognosis of breast cancer patients.[21] TROJAN has a low abundance of 246–361 copies per cell in certain cell lines,[22] which is a challenge for early cancer detection and diagnosis. This is one of the reasons that few sensing methods have been developed to quantify TROJAN.

Among the different electrochemical methods, photoelectrochemical (PEC) detection is an attractive variant owing to its superior sensitivity.[23] A key step in the PEC detection is the efficient separation of the photogenerated holes from their electron counterpart. This aspect is the same as that essential to the performance of photocatalysts,[24] photoelectronic components,[25,26] and memory devices.[26] Hence, for enhancing their performance, different types of heterojunctions have been developed.[25,26] Type II heterojunction is arguably one of the most widely used in the aforementioned applications because its staggered band structure affords a better spatial hole/electron separation than type I heterojunction and others.[24,27] We should note that the lowered redox activity of type II heterojunctions are not problematic in the PEC detection because an easily oxidizable species can be added into the sample solution according to the valence band position. Although a number of heterojunctions have also been incorporated in the PEC detection, the predominant ones are constructed with two inorganic compounds of different bandgaps. Attaching heterojunctions synthesized *ex situ* to the substrate electrode for PEC detection is generally inconvenient or not highly controllable. For those that can be produced *in situ*, the preparative method

[a]*School of Life Sciences, Tiangong University, Tianjin, P. R. China. E-mail: pxh1118@yeah.net; zhoufeimeng@tiangong.edu.cn; Fax: +1-323-343-6490; Tel: +1-323-343-2390; +86-22-839-55-665*

[b]*College of Chemistry, Chemical Engineering and Materials Science, Shandong Normal University, Jinan, Shandong, P. R. China*

[c]*Department of Obstetrics and Gynecology, Qilu Hospital of Shandong University, Jinan, Shandong, P. R. China. E-mail: yingxinpang@126.com*

[d]*Key Laboratory of Interfacial Reaction & Sensing Analysis in Universities of Shandong, School of Chemistry and Chemical Engineering, University of Jinan, Jinan, Shandong, P. R. China*

† Electronic supplementary information (ESI) available. See DOI: https://doi.org/10.1039/d4ra05238b

(*e.g.*, chemical vapor deposition[28,29]) is cumbersome or requires expensive devices (*e.g.*, atomic layer deposition[30]). Moreover, for heterogeneous biosensors requiring pre-immobilized capture probes, heterojunctions based on inorganic compounds need to be modified with an organic or polymeric layer to afford anchoring sites. We envision that an inorganic/organic heterojunction constructed *in situ* should be advantageous because (1) the same instrument used for the PEC detection can also be used to electrodeposit the heterojunction constituents, reducing the assay cost; (2) the preparation is straightforward and controllable; and (3) if the organic compound is the topmost layer, it can be functionalized for subsequent probe attachment. Furthermore, if the organic layer is a conducting polymer, the photogenerated electrons can rapidly transfer inside because of the good conductivity.

In this work, we constructed *in situ* a type II heterojunction *via* sequential electrodepositions of Cu_2O and poly-2,2,5,2-terthiophene (pTTh) onto an indium tin oxide (ITO) electrode for sensitive PEC detection. Cu_2O is a p-type inorganic semiconductor[31] with a narrow bandgap and photosensitivity in the visible light region.[32] Poly-thiophene and its derivative such as pTTh are among the various polymers used for heterojunction fabrication and modification. However, each compound alone is not effective in preventing the hole/electron recombination. As demonstrated below, the underlying Cu_2O nanocubes are highly uniform and the upper pTTh film has a good surface coverage. Although heterojunctions comprising Cu_2O and conducting polymers have been firmly established as of type II, they have been mainly used in photocatalysis and photodevice fabrications.[33,34] For those used in (bio)chemical sensing, they were either not used in conjunction with the PEC detection[35,36] or needed further derivatization with a film to confer molecular recognition (*e.g.*, molecular imprinting matrices[37,38]) or yielding a detection signal specific to the target molecule. To the best of our knowledge, few studies have employed a conducting polymer-based heterojunction onto which probe molecules can be linked for sensitive detection of disease biomarkers. We measured the bandgap of this heterojunction with UV-visible spectroscopy and deduced the valence and conduction band positions of Cu_2O and pTTh through X-ray photoelectron spectroscopy (XPS) and Mott–Schottky measurements. The uniformity of deposited Cu_2O and the excellent pTTh coverage are effective in preventing the hole/electron recombination. The combination of hole/electron separation and immobilization of oligonucleotide probes resulted in a PEC sensor that can accurately detect lncRNA at fM levels, affording an alternative method for early typing diagnosis of triple-negative breast cancer.

2 Materials and methods

2.1. Reagents and materials

2,2,5,2-Terthiophene (TTh, 99.0%), acetonitrile, *N*-hydroxysuccinimide (NHS, ≥99.9%) and 1-ethyl-3-(3-dimethylaminopropyl) carbodiimide hydrochloride (EDC, 99.0%) were purchased from Aladdin Biochemical Technology Co., Ltd (Shanghai, China). Copper sulfate ($CuSO_4$, 98.0%) and lactic acid (85.0%) were acquired from Nine-Dinn Chemistry Co., Ltd (Shanghai, China). Lithium perchlorate ($LiClO_4$, AR, ≥99.0%) and sodium hydroxide (NaOH, AR, ≥99.0%) were obtained from Sinopharm Group Chemical Reagent Co., Ltd (Beijing, China). 3-Mercaptopropionic acid (MPA, 99.0%) and sodium chloride (NaCl, 99.8%) were purchased from Shanghai Macklin Biochemical Co., Ltd Indium tin oxide (ITO)-coated glass substrates were obtained from Zhuhai Kaivo Optoelectronic Technology Co., Ltd (Zhuhai, China). All lncRNAs were synthesized by BoShang Biotech Co., Ltd (Shanghai, China). The RNeasy Plus Mini Kit was purchased from Qiagen Co., Ltd (German).

2.2. Equipment

X-ray diffraction (XRD) patterns were collected from a smart lab se X-ray diffractometer (Japan Electric Equipment Co., Ltd, Beijing, China). The elemental analysis data were obtained from an Escalab 250Xi X-ray photoelectron spectroscopic instrument (Seymour Fisher Technology Co., Ltd, Waltham, Massachusetts, USA). Fourier transform-infrared spectra (FT-IR) were recorded with a Bruker-Alpha infrared spectrometer (Bruker Co., Ltd, Billerica, Massachusetts, USA). Scanning electron microscopic (SEM) images and energy dispersive spectra (EDS) were acquired with an SU8010 microscope (Hitachi Co., Ltd, Tokyo, Japan). The TEM images were collected from a JEOL microscope (JEM-2100, Nippon Electronics Co., Ltd, Tokyo, Japan). Ultraviolet-visible absorption spectroscopy (UV-vis) spectra were obtained with a UV-Vis spectrophotometer (Shimadzu Instrument Co., Ltd, Suzhou, China).

2.3. Synthesis of the photoactive materials

Cu_2O were electrochemically deposited in a plating bath containing 0.4 M $CuSO_4$ and 3 M lactic acid.[39] Prior to the process, the electrode substrate was ultrasonically cleaned with acetone, isopropanol, ethanol, and water in sequence (40 min each). The pH value of the plating bath was adjusted to 11.0 with NaOH and the temperature was maintained at 60 °C. The potential was kept at −0.4 V (*vs.* Ag/AgCl) for 30 min. Finally, the substrate was rinsed with deionized water and dried at 37 °C.

pTTh films were electropolymerized onto Cu_2O. Specifically, the pTTh/Cu_2O heterojunction was prepared using cyclic voltammetry (CV) in an acetonitrile solution containing 10 mM TTh and 0.1 M $LiClO_4$. Ten CV cycles were conducted within the potential range from 0.0 to 1.2 V (*vs.* Ag/AgCl) at a scan rate of 25 mV s^{-1}. Each electrode was rinsed with acetonitrile and deionized water and dried in an oven at 37 °C.

2.4. PEC sensor construction

Each substrate electrode was coated with the pTTh/Cu_2O heterojunction and further modified through immersion in a 0.5 mL 0.1 M phosphate buffer saline (PBS) buffer containing 0.1 M NaCl and 3 mM MPA at 37 °C for 2 h. This was then followed by dipping the electrode in a solution containing the for TROJAN probe (C = 1.0 μM) and the EDC/NHS mixture at 37 °C for 30 min. Subsequently, each electrode was rinsed thoroughly with PBS buffer and deionized water to rid the

surface of unlinked TROJAN probe molecules. To detect TROJAN, each electrode was exposed to different concentrations of TROJAN at 37 °C for 2 h, and the surface was rinsed with PBS and deionized water. The sequence of the TROJAN probe for TROJAN is 5′-NH_2-ACA AGT GTG AGT TGA CTG GAA GTC TGA GAG GGA AAG TCC CCT CTA GAG TA-3′.

2.5. PEC measurements

All electrochemical measurements were carried out on a CHI850D electrochemical workstation (ChenHua Instruments Co., Ltd, Shanghai, China). The photoelectrochemical measurements were conducted in a three-electrode cell. An Ag/AgCl electrode (saturated KCl) and a Pt wire electrode served as the reference and auxiliary electrodes, respectively. A PBS buffer comprising 0.1 M ascorbic acid (AA) as the hole scavenger was found to be the best, because in it a high photocurrent can be generated (panel A in Fig. S1†). Glucose (0.05 M) was also added to maintain a steady flow of photocurrent (panels B–D in Fig. S1†).

The light source was a CEL-LED 100-WL white LED (Zhongjiao Jinyuan Technology Co., Ltd, Beijing, China). The irradiation wavelength was set at 430 nm with an exposure time of 25 s and a bias voltage of −0.1 V.

Total RNA was isolated from MCF7 cells using a RNeasy Plus Mini Kit (QIAGEN) following the manufacturer's protocol.

3 Results and discussion

3.1. Sensor design

Scheme 1 shows the construction of our PEC sensor. Briefly, Cu_2O is electrodeposited on an ITO substrate, with the follow-up *in situ* electropolymerization of TTh. As demonstrated by the data below, the electropolymerized pTTh film forms a type II heterojunction with Cu_2O for efficient electron delocalization. Prior to sample analyses, MPA molecules are allowed to adsorb for the follow-up probe immobilization (Fig. S2†). This is followed by crosslink of the probe molecules and the duplex formation with the TROJAN target. The number of DNA/RNA duplexes formed is dependent on the target concentration. As the TROJAN concentration increases, the photocurrent signal continually decreases from the baseline current (J_1), because the higher the density of the DNA/RNA duplexes, the greater extent of the blockage of the

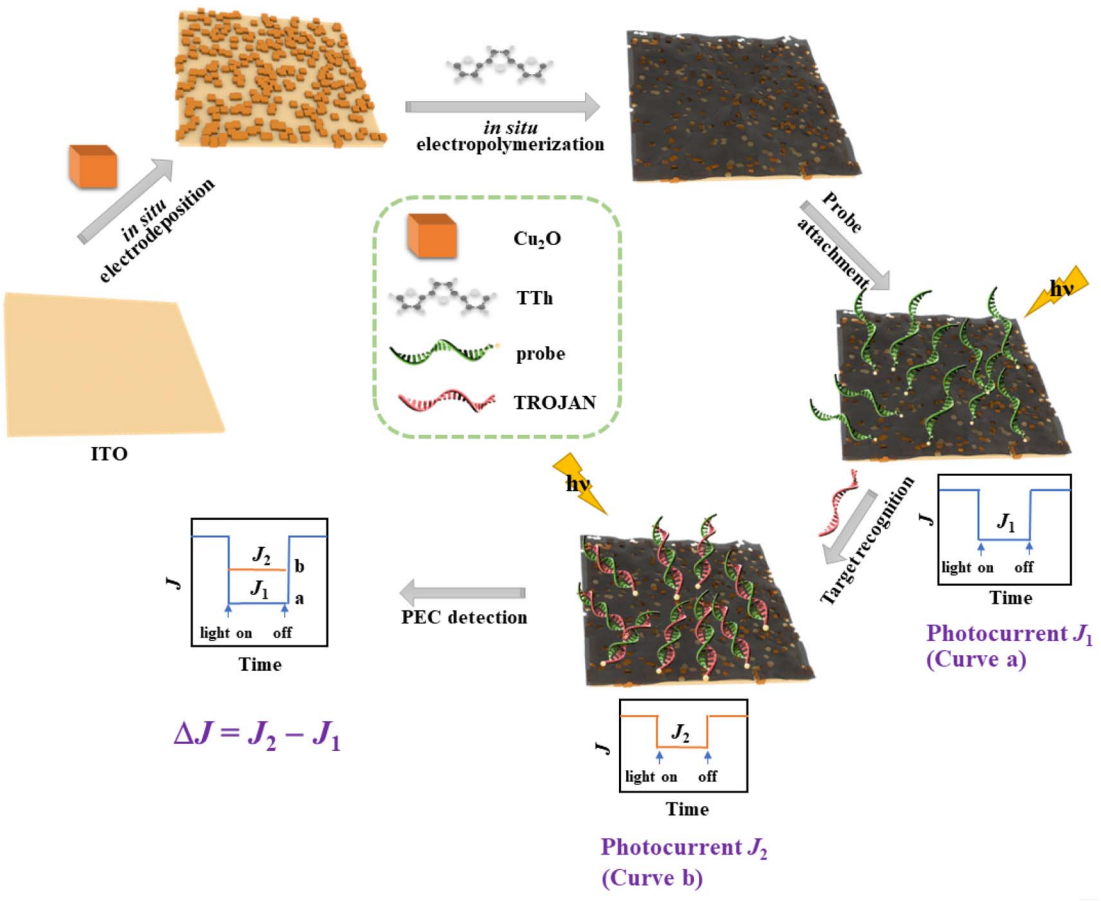

Scheme 1 Schematic illustration of the PEC sensor construction and its use for detecting the exosomal TROJAN target. In the PEC measurement, curve *a* represents the baseline photocurrent at the probe-covered pTTh/Cu_2O biosensor (J_1), which is reduced to J_2 when the probe molecule forms a duplex with the target (curve *b*). The difference, $\Delta J = J_2 - J_1$, is used to construct the calibration curve and sample quantification. The holes accumulated in Cu_2O can oxidize an oxidizable solution species penetrated through the pores of pTTh, while the photoelectrons are separated into pTTh and transferred to the ITO substrate through the pTTh/ITO interface.

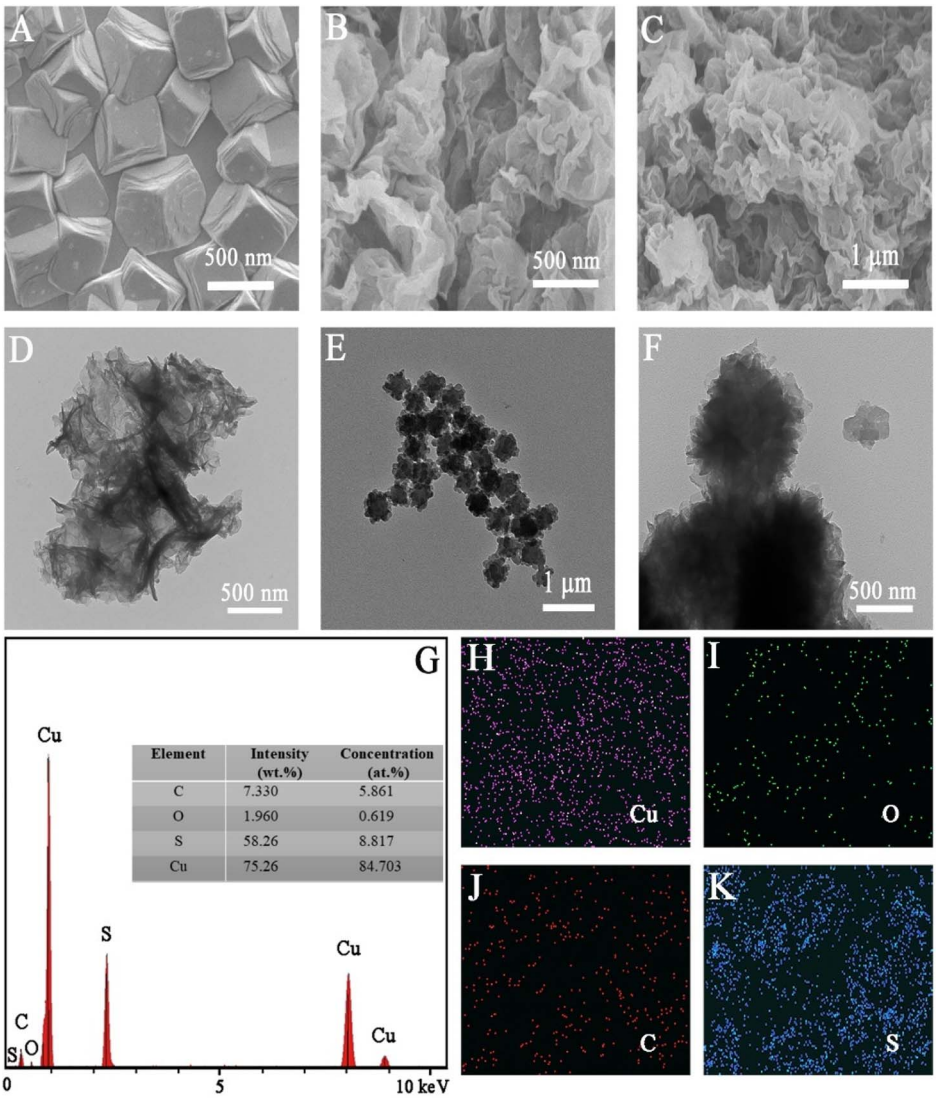

Fig. 1 SEM images of (A) Cu_2O, (B) pTTh, and (C) pTTh/Cu_2O. The TEM images of (D) pTTh and (E) pTTh/Cu_2O are shown. The TEM image of pTTh/Cu_2O shown in (F) is in higher resolution. (G) EDS and elemental mapping images of (H) Cu, (I) O, (J) C and (K) S of pTTh/Cu_2O.

receiving of photoholes by the redox species penetrated to the pores of pTTh from solution (a characteristic of an "off-sensor"). The excellent reproducibility described in the section below suggests that our sensor preparation is highly controllable. With the same potentiostat used for the PEC detection, our sensor fabrication is also cost-effective.

3.2. Characterizations of pTTh/Cu_2O

The surface morphologies of the electrodeposited pTTh, Cu_2O, and pTTh/Cu_2O were initially examined by SEM. In Fig. 1A depicts some highly uniform Cu_2O cubes, whose length is around 500 nm, while Fig. 1B shows that the pTTh film illustrates a pleated structure with a large specific surface area. Owing to this uniform and tight coverage, the diffusion length of the photogenerated carriers is shortened, allowing the photogenerated holes at pTTh to readily move to the underlying Cu_2O tubes and be effectively separated from the photoelectrons.[40]

The surface morphology and structure of pTTh/Cu_2O were also examined with TEM and compared to those of the individual constituents. Fig. 1D confirms that pTTh is indeed a pleated, amorphous film. Fig. 1E and F indicate that the length of the Cu_2O cube is consistent with the SEM result (Fig. 1B). The pTTh film completely enveloped the Cu_2O cube as well as the gaps between the Cu_2O tubes (see also Scheme 1). Fig. 1G reveals the coexistence of Cu, O, C, and S, while Fig. 1H–K suggest that these four elements are evenly distributed throughout the pTTh/Cu_2O heterojunction.

The crystal structure and surface composition of the heterojunction materials were analyzed with XRD and XPS. The XRD pattern in Fig. 2A shows that Cu_2O has the typical cuprite diffraction (JCPDS no. 05-0667) at 29.6°, 36.4°, 42.3°, 61.4°, and 73.5°, corresponding to the (110), (111), (200), (220) and (311) crystal planes.[41] In Fig. 2A, the peaks in the XRD pattern are characteristic of diffuse scattering and can be attributed to the amorphous feature of the polymer.

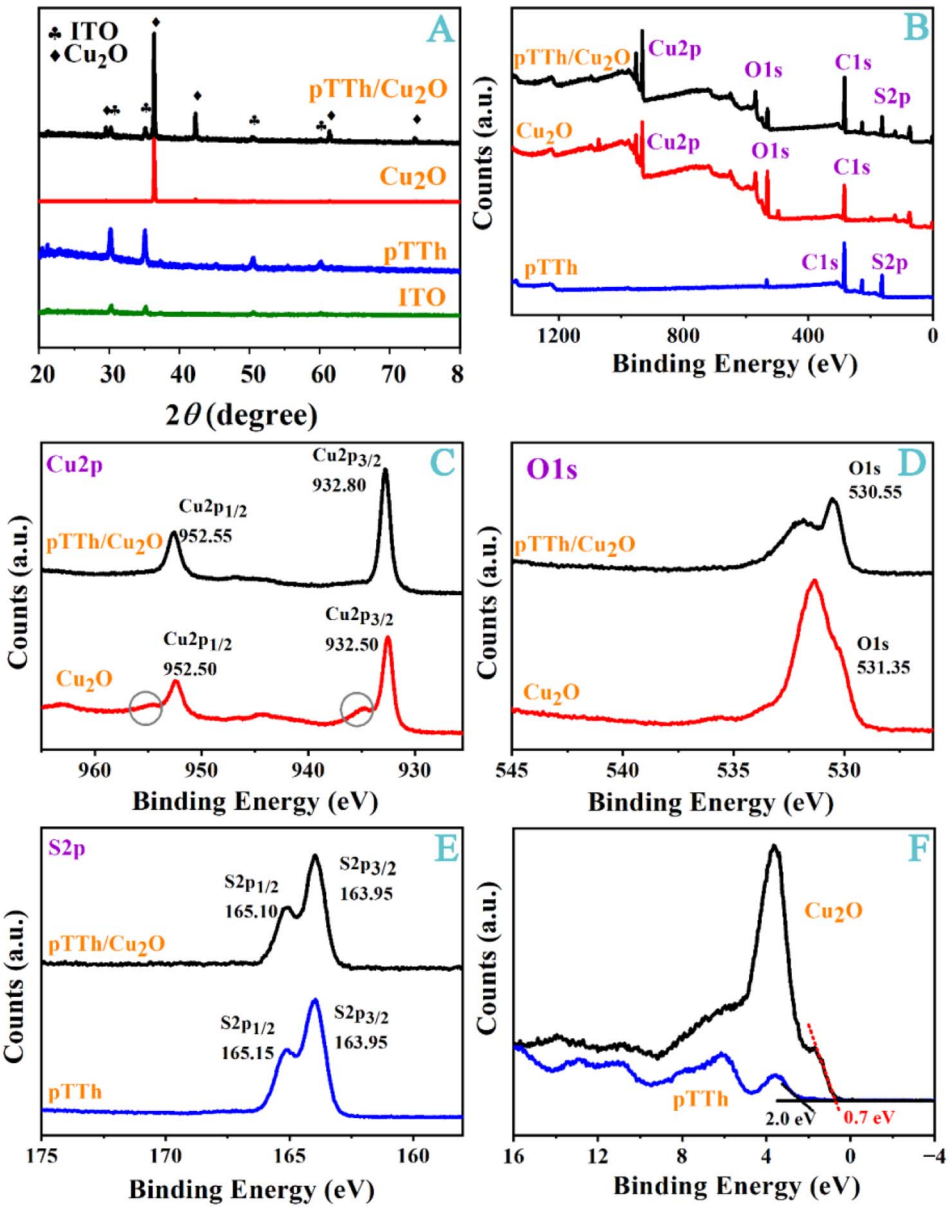

Fig. 2 (A) XRD patterns, (B) a full-scan XPS spectrum, and the corresponding narrow scan XPS spectra of (C) Cu2p, (D) O1s, and (E) S2p. (F) Valence band edge spectra of pTTh and pTTh/Cu_2O are shown.

In Fig. 2B, only the peak characteristic of Cu2p, O1s and C1s can be seen in the full-scan XPS spectra of Cu_2O. The additional S2p peak in the pTTh/Cu_2O heterojunction verifies the successful deposition of the pTTh film onto Cu_2O. The $Cu2p_{3/2}$ and $Cu2p_{1/2}$ peaks of Cu_2O can be found at 932.50 and 952.50 eV in Fig. 2C, respectively. Two small peaks, indicative of slight Cu_2O oxidation,[34] are present in the regions of 953–957 and 933–937 eV; however, they are absent in the XPS spectra of pTTh/Cu_2O. Thus, the pTTh film is impermeable to oxygen in solution. Even though the pTTh film is amorphous and porous, its hydrophilicity prevents O_2, which is more hydrophobic, from reaching the underlying Cu_2O tubes. The electrochemically active surface area (ECSA) of this heterojunction was measured to be 1.81 cm^2 (Fig. S3†), which is greater than the geometric area of the electrode (1.5 cm^2). Therefore, the heterojunction formed on the substrate electrode also increased the reactive surface area.

As shown in Fig. 2D, the O1s peak is located at 531.35 eV with a broad peak, which is attributable to the hydroxyl groups (531.61 eV) adsorbed on the Cu_2O surface.[42] The O1s peak of pTTh/Cu_2O shifts slightly to 530.55 eV after the pTTh formation, because pTTh reduces the O1s binding energy of the hydroxyl groups on the Cu_2O surface. As shown in Fig. 2E, the peaks of $S2p_{3/2}$ and $S2p_{1/2}$ are located at 163.95 and 165.15 eV, consistent with the literature data.[43] The $S2p_{3/2}$ and $S2p_{1/2}$ peaks are at 163.95 and 165.10 eV, respectively. The positions of the valence bands (VB) of Cu_2O (0.7 eV) and pTTh (2.0 eV) were determined through linear extrapolation fitting of the XPS data

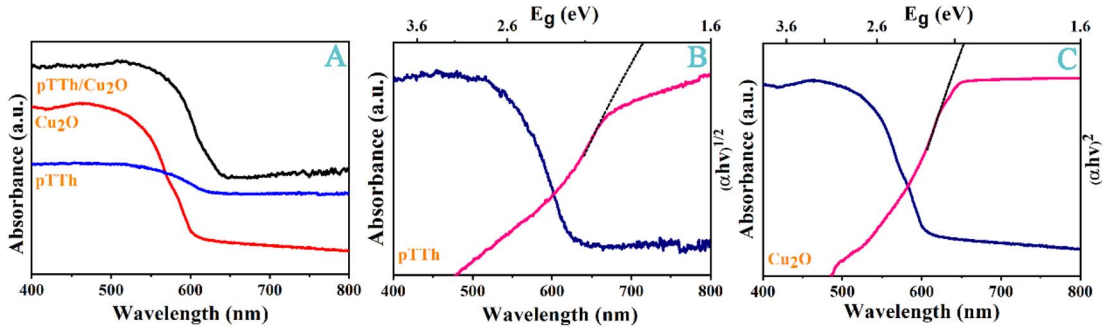

Fig. 3 (A) UV-vis spectra for the heterojunction and its constituents. The Tauc plot (red) calculated from the absorption spectrum (blue) of (B) pTTh and (C) Cu_2O are also shown.

presented in Fig. 2F. The results are consistent with those deduced from our Mott–Schottky measurements (Fig. S4†).

The optical properties of Cu_2O, pTTh, and pTTh/Cu_2O were further characterized with UV-vis spectroscopy (Fig. 3A). The optical absorption edge of pTTh is 620 nm. A bandgap energy of 1.9 eV for pTTh was deduced from normalization and Tauc fitting of the spectrum in Fig. 3B.[44] For Cu_2O, the optical absorption edge is 610 nm, which greatly attenuates in the range of 500–600 nm. Similarly, the bandgap of Cu_2O was deduced from Fig. 3C to be 2.1 eV, in agreement with the literature value.[45] The conduction bands (CB) are therefore around 0.1 and −1.4 eV for pTTh and Cu_2O, respectively. As mentioned in the Introduction, such a staggered band structure favors the separation of photoelectrons. Apparently, a sensitization effect exists between the pTTh and Cu_2O, which widens the range of visible light absorption.

3.3. Performance and the photovoltaic mechanism of the PEC sensor

As shown in Fig. 4A, pTTh and Cu_2O both have lower photoelectric activities when compared to that of pTTh/Cu_2O. The photocurrent density of pTTh is about −80 μA cm^{-2}, and that of Cu_2O is about −90 μA cm^{-2}. By contrast, the photocurrent density of the pTTh/Cu_2O was augmented to −250 μA cm^{-2}. This increase can be again ascribed to the staggered band

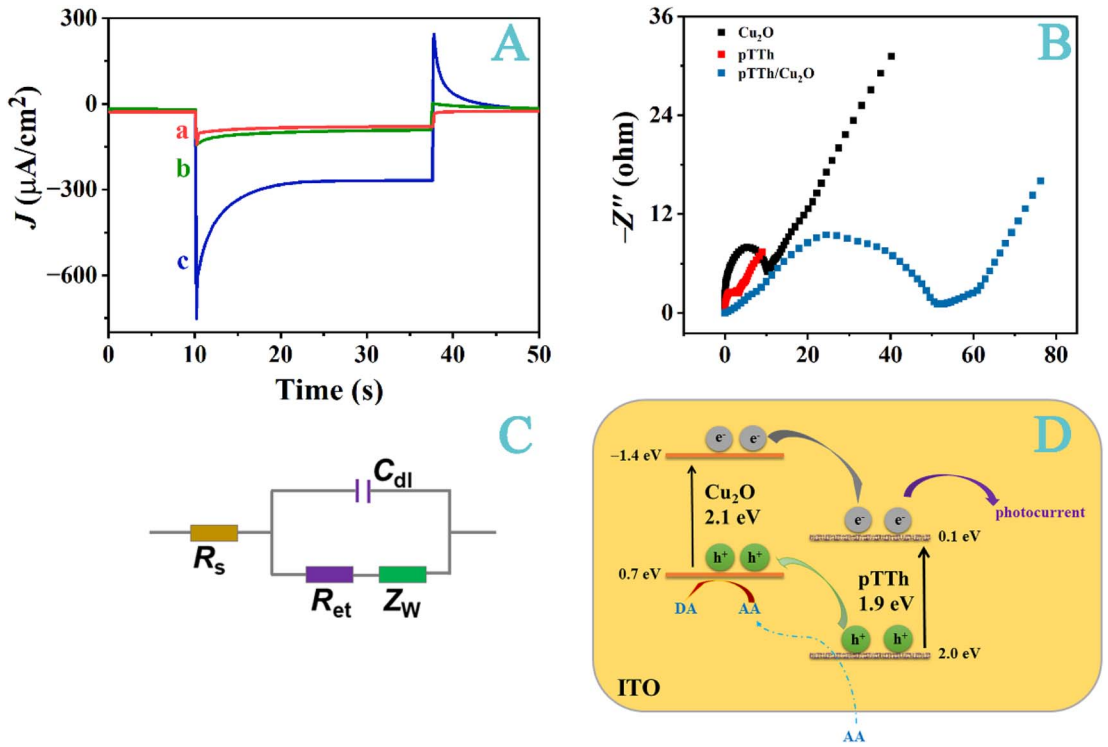

Fig. 4 Signal responses at (a) pTTh, (b) Cu_2O, and (c) pTTh/Cu_2O (A), Nyquist plots of pTTh, Cu_2O, and pTTh/Cu_2O (B), as well as the Randles equivalent circuit (C), are presented. Additionally, (D) a schematic depiction of the mechanism behind the photocurrent generation is shown, including the band energy values and bandgap. AA added in the sample solution penetrate through the pores of pTTh (denoted by the red arrows) to the Cu_2O tubes and are oxidized to deoxyascorbic acid (DA) by the photogenerated holes.

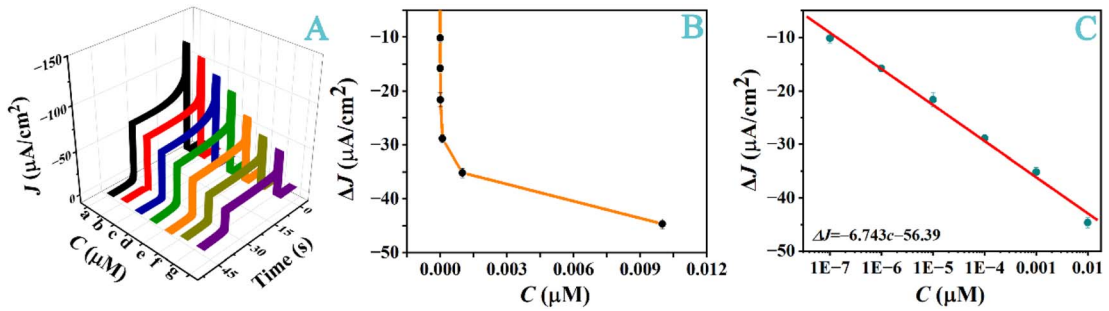

Fig. 5 (A) Photocurrent responses of the PEC sensor to different concentrations of TROJAN (a: blank and baseline current and b to g: 10 nM to 0.1 pM and their corresponding currents). (B) ΔJ plotted against concentration. (C) ΔJ plotted as a function of log C. The error bars are relative standard deviations (RSDs) of three replicates.

structure that inhibits the hole/electron recombination.[46] We should add that the resonance structure of pTTh helps delocalize the photogenerated electrons (the electron/hole lifetime of Cu_2O has been reported to be only 1 ps (ref. 47)), further limiting the hole/electron recombination. This effect of the heterojunction on prolonging the photoelectron lifetime is reflected from the Nyquist plots shown in Fig. 4B and the equivalent circuit depicted in Fig. 4C. The values of R_{et} (charge transfer resistance) are 2.6 Ω for pTTh, 10.6 Ω for Cu_2O and 51.5 Ω for pTTh/Cu_2O. Concurrently, C_{dl} (double-layer capacitance) also increases in the same order (see also values summarized in Table S1†). Linear sweep voltammetry (LSV, Fig. S5†) and incident photon-to-current conversion efficiency (IPCE, Fig. S6†) measurements directly demonstrate that the formation of this heterojunction enhances the photoactivity and accelerates the separation of the photogenerated electron–hole pairs. The IPCE values range from 13 to 32% within 360–700 nm and are higher in the visible region than some other reports.[27]

Fig. 4D depicts the mechanism behind the photocurrent generation. In a type II heterojunction, upon light irradiation, the electrons are accumulated in the CB of pTTh[44] while the photogenerated holes are concentrated in the VB of Cu_2O.[45] The photogenerated holes will oxidize an easily oxidizable species in the solution. It is likely that AA, being hydrophilic, should be able to diffuse through the pTTh pores to reach the Cu_2O tubes. Concurrently, electrons accumulated in the pTTh flow through the area in contact with the substrate electrode to produce the photocurrent (see also Scheme 1).[27] Thus, the heterojunction separates the holes from their electron counterparts into different materials and the spatial separation impedes the recombination.[33,39,48–50] Notice that the redox capability is compromised with a heterojunction. However, this is not an issue in the PEC detection because an additive more readily oxidizable than AA can be used if the oxidation potential is lowered.

We assessed the feasibility of our method for quantifying lncRNA TROJAN (Fig. 5). The performance of this sensor was first evaluated after the functionalization of this sensor (Fig. S7†). As depicted in Fig. 5A, the photocurrent decreases as the TROJAN concentration is below 1.0 nM and begins to plateau thereafter, after most of the anchored probe molecules have formed duplexes with the target molecules. This behavior is typical of a heterogeneous sensor whereon the amount of analyte adsorption is directly proportional to the concentration when the surface coverage is low. When the adsorption amount is high, more incident light is blocked and less AA molecules can move closer to the Cu_2O tubes to annihilate the photoholes. These two factors jointly decrease the amount of photoelectrons or photocurrent.

Fig. 5B plots the decreases of the photocurrents with respect to the baseline value of the blank solution (ΔJ) against the TROJAN concentration, while Fig. 5C shows that ΔJ is proportional to the logarithm of the TROJAN concentration, log C, within the concentration range of 0.1–10 000 pM. The linear regression equation is $\Delta J = -6.743 \log C - 56.39$, with a linear

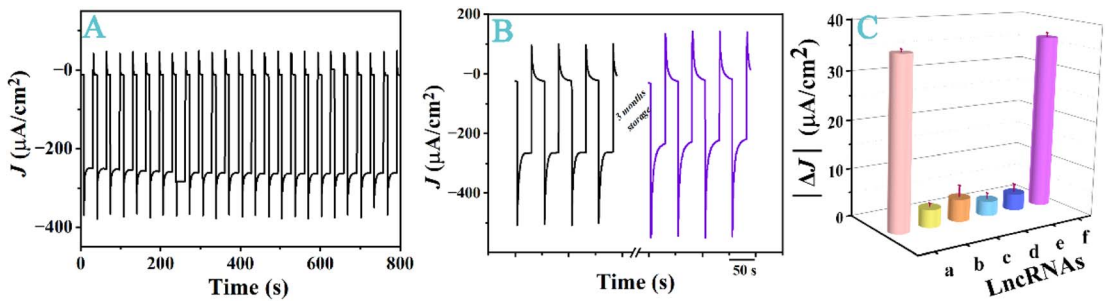

Fig. 6 (A) Repeatability of the PEC sensor, (B) storage life of the heterojunction in dry state, and (C) selectivity of the PEC sensor for detecting TROJAN (1 nM) in (a) a buffer and (b) buffer solutions containing L1 (1 nM), (c) ANCR (1 nM), (d) UCA1 (1 nM), (e) BCRT1 (1 nM), and the mixture of these additives (f, 1 nM each).

correlation coefficient of $R^2 = 0.9934$. Using the lower portion of the curve in Fig. 5B and a signal-to-noise ratio that is higher than three folds of the noise level (S/N $\geq$ 3), we gauged the detection limit of our PEC sensor to be 15.8 fM. Such a level compares well with those attainable with many previously reported methods (Table S2†). We should note that some recent work, based on polarity-switching PEC sensors for lncRNA detections, have achieved sensitivity levels down to low fM or to even aM levels.[12,13] Although the polarity-switching strategy involves complicated sensor fabrication and detection procedures, superb sensitivity can be attained because of the much enhanced signal-to-noise ratio. Using the diameter of a typical breast cancer cell (about 10 μm (ref. 51)), one copy of lncRNA corresponds to about 3 pM in the interior of such a cancer cell. Because the expression level of TROJAN is in the hundreds, our sensor is more than adequate for measuring the low abundance of this cancer biomarker.[22] Indeed, we found that our method can easily measure the amount of TROJAN lncRNAs in MCF7 cells (*vide infra*).

To assess the feasibility of our sensor for real-sample analysis, we evaluated its stability, selectivity, and reproducibility. As shown in Fig. 6A, the signals were continuously measured for 800 s in PBS with 24 irradiation on/off cycles. It is evident that the photocurrent response is highly repeatable, with an RSD value of only 2.09%. We also stored electrodes covered with dry pTTh/Cu_2O at room temperature in dark for three months and measured signals for the same sample intermittently. As shown by the representative data in Fig. 6B, the storage life is as long as three months. We opted to store the heterojunction-covered electrodes instead of the probe-covered sensors because MPA used to anchor the probe molecules is prone to oxidation.[52] The stability and reproducibility exhibited in Fig. 6B indicate that it is a viable approach as the MPA adsorption and probe immobilization are apparently repeatable under the same experimental condition. To assess the selectivity, we measured a buffer solution containing 1.0 nM TROJAN and compared the signal to those from solutions with the ANCR, BCRT1, UCA1, L1 gene fragments and their mixture as additives. ANCR[53] and BCRT1 (ref. 54) are lncRNAs linked to the etiology of the triple-negative breast cancer, while UCA1 (ref. 55) and L1 (ref. 56) are gene markers of colon cancer. As shown in Fig. 6C, our sensor did not show a significant attenuation of photocurrent in the presence of these fragments, suggesting that the additives did not adsorb nonspecifically onto the sensor surface. In fact, the recovery rate of the sample with these lncRNAs is 102 $\pm$ 2%. To further demonstrate the suitability of our sensor for real sample analyses, we measured lncRNA TROJAN extracted from MCF7 tumor cells, and found that the lncRNA TROJAN was at 480 pM corresponding to the literature,[22] with a RSD value of 1.45%.

The aforementioned features, along with the fact that small ITO substrates can be mass-produced, render the possibility of fabricating our PEC sensors as of the disposable kind. Finally, we gauged the sensor-to-sensor reproducibility by employing 25 sensors to measure the same sample. The resulting RSD value, 2.35%, is exceedingly low. This again indicates that the *in situ* electrodepositions, as well as the follow-up MPA adsorption and probe immobilization are controllable in producing PEC sensors of consistent composition and structure.

4 Conclusion

We have developed a sensitive PEC sensor for reproducible and reliable lncRNA detection. Sequential electrodepositions of Cu_2O and pTTh produced a type II heterojunction structure at an ITO substrate. Owing to the uniform coverage and tight contact of pTTh, the heterojunction is not only highly stable (preventing the underlying Cu_2O from oxidation), but also effective in accelerating the photoelectron transfer and enhancing the photocurrent. Furthermore, the use of pTTh facilitates the affixation of oligonucleotide probe molecules. We demonstrate that the judicious choice of inorganic and polymeric materials, in conjunction with simple yet reproducible surface preparative methods, can lead to a wide linear range with a remarkably low detection limit. These are prerequisites for robust detections of biomarkers at ultratrace levels in clinical settings. Thus, our method can be easily extended to the immobilization of other types of biomolecules such as proteins and peptides, significantly expanding the range of biological applications of PEC biosensors based on the inorganic/conductive heterojunctions.

Data availability

The data for this article have been included in the manuscript and also as part of the ESI.†

Author contributions

Xuehui Pang, Xiaoyi Lv, Yingxin Pang, Zhen Li, Qing Kang, Rui Liu, and Jiandong Xie performed experiments. Wenjun Lu, Lebin Sun, Qiuyan Wang. Rui Liu, and Jiandong Xie conducted some data analysis. Pang and Feimeng Zhou conceptualized the work and wrote the manuscript.

Conflicts of interest

The authors declare that they have no known competing financial interests or personal relationships that could have appeared to influence the work reported in this paper.

Acknowledgements

This work was supported by The Program of Science and Technology Plan of the City of Tianjin (No. 24JRRCRC00040), the National Natural Science Foundation of China (No. 21904081 and No. 81902657), and a grant from the start-up funds provided by Tiangong University.

References

1 D. Nandi, S. Parida and D. Sharma, *Gut Microbes*, 2023, **15**, 2221452.
2 T. Sorlie, C. M. Perou, R. Tibshirani, T. Aas, S. Geisler, H. Johnsen, T. Hastie, M. B. Eisen, M. van de Rijn, S. S. Jeffrey, T. Thorsen, H. Quist, J. C. Matese,

P. O. Brown, D. Botstein, P. E. Lonning and A. L. Borresen-Dale, *Proc. Natl. Acad. Sci. U. S. A.*, 2001, **98**, 10869–10874.
3 J. Lengfeld, H. T. Zhang, S. Stoesz, R. Murali, F. Pass, M. I. Greene, P. N. Goel and P. Grover, *Breast Cancer*, 2021, **13**, 575–593.
4 H. You, M. Wang, S. Wang, J. Xu, S. H. Hu, T. H. Li, Z. Z. Yu, D. P. Tang and N. Gan, *Anal. Chem.*, 2023, **95**, 11211–11218.
5 Z. Wang, L. Balembois, M. Rančić, E. Billaud, M. Le Dantec, A. Ferrier, P. Goldner, S. Bertaina, T. Chanelière, D. Esteve, D. Vion, P. Bertet and E. Flurin, *Nature*, 2023, **619**, 276–281.
6 X. Bi, D. M. Czajkowsky, Z. Shao and J. Ye, *Nature*, 2024, **628**, 771–775.
7 R. Ni, K. Ge, Y. Luo, T. Zhu, Z. Hu, M. Li, P. Tao, J. Chi, G. Li, H. Yuan, Q. Pang, W. Gao, P. Zhang and Y. Zhu, *Biosens. Bioelectron.*, 2024, **264**, 116616.
8 N. Debnath, L. S. Live and M. Poudineh, *Lab Chip*, 2023, **23**, 572–579.
9 H. Liu, Y. Wang, S. Huang, J. Tai, X. Wang, X. Dai, C. Qiu, D. Gu, W. Yuan, H.-P. Ho, J. Chen and Y. Shao, *Anal. Chem.*, 2024, **96**, 8791–8799.
10 L. Cui, J. Shen, C.-C. Li, P.-P. Cui, X. Luo, X. Wang and C.-Y. Zhang, *Anal. Chem.*, 2021, **93**, 10310–10316.
11 X. H. Pang, X. Zhang, K. K. Gao, S. Wan, C. Cui, L. Li, H. B. Si, B. Tang and W. H. Tan, *ACS Nano*, 2019, **13**, 1817–1827.
12 R. Yang, J. Ji, L. Ding, X. Yuan, L. Qu, Y. Wu and Y. Li, *Anal. Chem.*, 2024, **96**, 13278–13284.
13 Y. Li, L.-e. Liu, H. Han, X. Yuan, J. Ji, L. Xue, Y. Wu and R. Yang, *Talanta*, 2024, **273**, 125878.
14 M. Zuo, Y. Yang, S. Jiang, C. Zhu, Y. Han, J. Hu, K. Ren, L. Cui and C.-Y. Zhang, *Food Chem.*, 2024, **445**, 138716.
15 J. Yin, Z. Zou, F. Yin, H. Liang, Z. Hu, W. Fang, S. Lv, T. Zhang, B. Wang and Y. Mu, *ACS Nano*, 2020, **14**, 10385–10393.
16 Y. Zhang, C. Wang, X. Zou, X. Tian, J. Hu and C.-y. Zhang, *Nano Lett.*, 2021, **21**, 4193–4201.
17 W.-j. Liu, L. Zhang and C.-y. Zhang, *Anal. Chem.*, 2023, **95**, 16343–16351.
18 S. Jiang, T. Liu, Q. Liu, Q. Zhang, Y. Han, X. Tian and C.-y. Zhang, *Anal. Chem.*, 2023, **95**, 15133–15139.
19 C. Jiang, X. Li, H. Zhao and H. Liu, *Mol. Cancer*, 2016, **15**, 62.
20 X. Jin, L. Ge, D. Li, Z. Shao, G. Di, X. Xu and Y.-Z. Jiang, *Mol. Cancer*, 2020, **19**, 87.
21 K. K. Thakur, A. Kumar, K. Banik, E. Verma, E. Khatoon, C. Harsha, G. Sethi, S. C. Gupta and A. B. Kunnumakkara, *J. Cell. Physiol.*, 2021, **236**, 7938–7965.
22 X. Jin, X. Xu, Y. Jiang, Y. Liu, W. Sun, Y. Guo, Y. Ren, W. Zuo, X. Hu, S. Huang, H. Shen, F. Lan, Y. He, G. Hu, G. Di, X. He, D. Li, S. Liu, K. Yu and Z. Shao, *Sci. Adv.*, 2019, **5**, eaat9820.
23 X. H. Pang, C. Cui, M. H. Su, Y. G. Wang, Q. Wei and W. H. Tan, *Nano Energy*, 2018, **46**, 101–109.
24 J. X. Low, J. G. Yu, M. Jaroniec, S. Wageh and A. A. Al-Ghamdi, *Adv. Mater.*, 2017, **29**, 1601694.
25 F. H. Chu, X. L. Qu, Y. C. He, W. L. Li, X. Q. Chen, Z. L. Zheng, M. Yang, X. N. Ru, F. G. Peng, M. H. Qu, K. Zheng, X. X. Xu, H. Yan and Y. Z. Zhang, *Nat. Commun.*, 2023, **14**, 3596.
26 X. Y. Huang, L. M. Zhang, L. Tong, Z. Li, Z. R. Peng, R. F. Lin, W. H. Shi, K. H. Xue, H. W. Dai, H. Cheng, D. D. Branco, J. B. Xu, J. B. Han, G. J. Cheng, X. S. Miao and L. Ye, *Nat. Commun.*, 2023, **14**, 2190.
27 Y. Wang, H. Shi, K. Cui and J. Yu, *Appl. Catal., B*, 2019, **250**, 171–180.
28 J. L. Fan, X. F. Hu, W. W. Qin, Z. Y. Liu, Y. S. Liu, S. J. Gao, L. P. Tan, J. L. Yang, L. B. Luo and W. Zhang, *Nanoscale*, 2022, **14**, 13204–13213.
29 Y. M. Kou, L. D. Chen, J. L. Mu, H. Miao, Y. S. Wang, X. Y. Hu and F. Teng, *Nanotechnology*, 2020, **31**, 195601.
30 X. H. Zhou, R. Liu, K. Sun, K. M. Papadantonakis, B. S. Brunschwig and N. S. Lewis, *Energy Environ. Sci.*, 2016, **9**, 892–897.
31 X. Deng, R. Li, S. Wu, L. Wang, J. Hu, J. Ma, W. Jiang, N. Zhang, X. Zheng, C. Gao, L. Wang, Q. Zhang, J. Zhu and Y. Xiong, *J. Am. Chem. Soc.*, 2019, **141**, 10924–10929.
32 D. Barreca, P. Fornasiero, A. Gasparotto, V. Gombac, C. Maccato, T. Montini and E. Tondello, *ChemSusChem*, 2009, **2**, 230–233.
33 X. Chang, T. Wang, P. Zhang, Y. Wei, J. Zhao and J. Gong, *Angew. Chem., Int. Ed.*, 2016, **55**, 8840–8845.
34 W. Niu, T. Moehl, P. Adams, X. Zhang, R. Lefèvre, A. M. Cruz, P. Zeng, K. Kunze, W. Yang and S. D. Tilley, *Energy Environ. Sci.*, 2022, **15**, 2002–2010.
35 H. Ullah, R. Ahmad, A. A. Khan, N. E. Lee, J. Lee, A. U. Shah, M. Khan, T. Ali, G. Ali, Q. Khan and S. O. Cho, *ACS Omega*, 2022, **7**, 42377–42395.
36 Y. Zhao, L. Fan, Y. Zhang, H. Zhao, X. Li, Y. Li, L. Wen, Z. Yan and Z. Huo, *ACS Appl. Mater. Interfaces*, 2015, **7**, 16802–16812.
37 K. Dashtian, S. Hajati and M. Ghaedi, *Anal. Chem.*, 2022, **94**, 6781–6790.
38 K. Dashtian, S. Hajati and M. Ghaedi, *Biosens. Bioelectron.*, 2020, **165**, 112346.
39 C. Yang, P. D. Tran, P. P. Boix, P. S. Bassi, N. Yantara, L. H. Wong and J. Barber, *Nanoscale*, 2014, **6**, 6506–6510.
40 S. W. Lee, Y. S. Lee, J. Heo, S. C. Siah, D. Chua, R. E. Brandt, S. B. Kim, J. P. Mailoa, T. Buonassisi and R. G. Gordon, *Adv. Energy Mater.*, 2014, **4**, 1301916.
41 Y. Li, X. Zhong, K. Luo and Z. Shao, *J. Mater. Chem. A*, 2019, **7**, 15593–15598.
42 H. Li, Z. Su, S. Hu and Y. Yan, *Appl. Catal., B*, 2017, **207**, 134–142.
43 K. Wang, Z. Mo, S. Tang, M. Li, H. Yang, B. Long, Y. Wang, S. Song and Y. Tong, *J. Mater. Chem. A*, 2019, **7**, 14129–14135.
44 W. Fan, B. Zhang, X. Wang, W. Ma, D. Li, Z. Wang, M. Dupuis, J. Shi, S. Liao and C. Li, *Energy Environ. Sci.*, 2020, **13**, 238–245.
45 A. Paracchino, N. Mathews, T. Hisatomi, M. Stefik, S. D. Tilley and M. Grätzel, *Energy Environ. Sci.*, 2012, **5**, 8673–8681.
46 W. Zhao, Y. Feng, H. Huang, P. Zhou, J. Li, L. Zhang, B. Dai, J. Xu, F. Zhu, N. Sheng and D. Y. C. Leung, *Appl. Catal., B*, 2019, **245**, 448–458.
47 M. A. Mahmoud, W. Qian and M. A. El-Sayed, *Nano Lett.*, 2011, **11**, 3285–3289.
48 W. Fan, C. Chen, H. Bai, B. Luo, H. Shen and W. Shi, *Appl. Catal., B*, 2016, **195**, 9–15.

49 C. Lin, Y. Lai, D. Mersch and E. Reisner, *Chem. Sci.*, 2012, **3**, 3482–3487.
50 J. Bai, Y. Li, R. Wang, K. Huang, Q. Zeng, J. Li and B. Zhou, *J. Mater. Chem. A*, 2015, **3**, 22996–23002.
51 K. Kyriakopoulou, E. Riti, Z. Piperigkou, K. K. Sarri, H. Bassiony, M. Franchi and N. K. Karamanos, *Cells*, 2020, **9**, 2256.
52 Q. Shen, L. Han, G. Fan, J.-R. Zhang, L. Jiang and J.-J. Zhu, *Anal. Chem.*, 2015, **87**, 4949–4956.
53 S. B. Wang, F. Lan and Y. Xia, *Med. Sci. Monit.*, 2018, **24**, 6002–6009.
54 G. Han, Q. Y. Guo, N. Ma, W. Z. Bi, M. Xu, J. P. Jia and W. Wang, *Aging*, 2021, **13**, 15501–15510.
55 M. H. Wang, Z. J. Zhang, D. Pan, Z. G. Xin, F. Bu, Y. Zhang, Q. W. Tian and X. D. Feng, *Biosci. Rep.*, 2021, **41**, BSR20211115.
56 **https://www.ncbi.nlm.nih.gov/nuccore/XR_927227.2/**.